The Ratio of Key Metabolic Transcripts Is a Predictive Biomarker of Breast Cancer Metastasis to the Lung

Deepti Mathur[1], Chen Liao[1], Wendy Lin[1], Alessandro La Ferlita[2], Salvatore Alaimo[3], Samuel Taylor[4,5], Yi Zhong[6,7], Christine Iacobuzio-Donahue[6], Alfredo Ferro[3], and Joao B. Xavier[1]

ABSTRACT

Understanding the rewired metabolism underlying organ-specific metastasis in breast cancer could help identify strategies to improve the treatment and prevention of metastatic disease. Here, we used a systems biology approach to compare metabolic fluxes used by parental breast cancer cells and their brain- and lung-homing derivatives. Divergent lineages had distinct, heritable metabolic fluxes. Lung-homing cells maintained high glycolytic flux despite low levels of glycolytic intermediates, constitutively activating a pathway sink into lactate. This strong Warburg effect was associated with a high ratio of lactate dehydrogenase (LDH) to pyruvate dehydrogenase (PDH) expression, which correlated with lung metastasis in patients with breast cancer. Although feature classification models trained on clinical characteristics alone were unable to predict tropism, the LDH/PDH ratio was a significant predictor of metastasis to the lung but not to other organs, independent of other transcriptomic signatures. High lactate efflux was also a trait in lung-homing metastatic pancreatic cancer cells, suggesting that lactate production may be a convergent phenotype in lung metastasis. Together, these analyses highlight the essential role that metabolism plays in organ-specific cancer metastasis and identify a putative biomarker for predicting lung metastasis in patients with breast cancer.

Significance: Lung-homing metastatic breast cancer cells express an elevated ratio of lactate dehydrogenase to pyruvate dehydrogenase, indicating that ratios of specific metabolic gene transcripts have potential as metabolic biomarkers for predicting organ-specific metastasis.

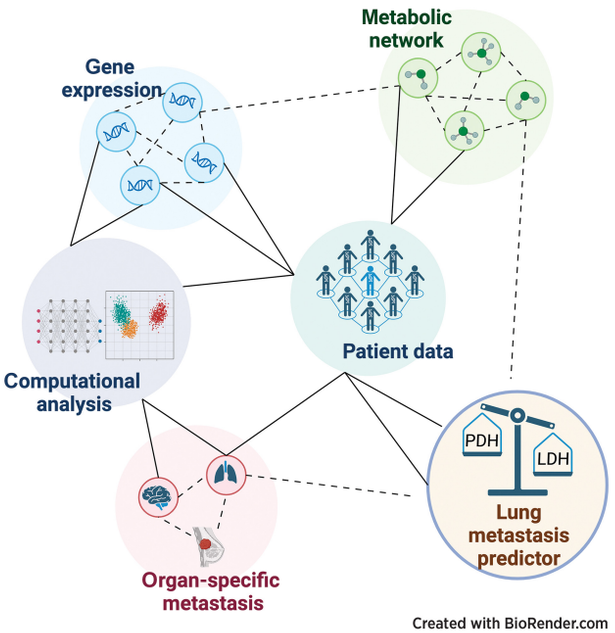

Introduction

Breast cancer is a disease marked by cellular diversity, and cancer cells from the same primary tumor can colonize multiple metastatic sites. Metastasis is a rare and stochastic process, and because of that it becomes very difficult to predict when, where, and whether a patient diagnosed with breast cancer will develop metastases and which organs will be affected (1). Cells that metastasize to different organs can express different levels of therapeutic targets (2, 3) and respond differently to treatment (4, 5). Understanding the molecular processes that drive metastatic tropism is therefore vital for the future of targeted therapy and prevention.

When a cancer cell disseminates from a breast tumor it may already have a propensity to metastasize to a specific organ (6–8). The possibility that the distal tissue selects for specific features of cancer cells was first raised by Paget, termed the "seed-and-soil hypothesis" (9). However, the cell phenotypes under selection in each organ remain unclear. Breast cancers are categorized by molecular subtypes defined by the presence of hormone receptors; these subtypes correlate modestly with preferential relapse sites, but still allow the possibility to

[1]Program for Computational and Systems Biology, Memorial Sloan-Kettering Cancer Center, New York, New York. [2]Department of Cancer Biology and Genetics, The James Comprehensive Cancer Center, The Ohio State University, Columbus, Ohio. [3]Department of Clinical and Experimental Medicine, Bioinformatics Unit, University of Catania, Catania, Italy. [4]Weill Cornell–Rockefeller–Sloan Kettering Tri-Institutional MD–PhD Program, New York, New York. [5]Department of Medicine, Brigham and Women's Hospital, Boston, Massachusetts. [6]Department of Pathology, Memorial Sloan-Kettering Cancer Center, New York, New York. [7]Hackensack Meridian Health Center for Discovery and Innovation, Nutley, New Jersey.

Corresponding Authors: Deepti Mathur, Computational and Systems Biology, Memorial Sloan Kettering Cancer Center, New York, NY 10065. E-mail: mathurd@mskcc.org; and Joao de Bivar Xavier, 417 E 68th Street, Room 1463, New York, NY 10065. E-mail: xavierj@mskcc.org

Cancer Res 2023;83:3478–91

doi: 10.1158/0008-5472.CAN-23-0153

metastasize to multiple sites (10–13). Histologic grade, defined by cell morphology, mitosis, and cellular differentiation state, also does not correlate well with tissue tropism (13). Oncogenic mutations found in driver genes are also used to type breast cancers, but these mutations remain fairly consistent between primary tumors and untreated metastases (14). It is therefore likely that metastatic tropism is determined by factors other than those used to type breast cancers at the clinical level.

Preclinical work has shown some of the other factors that command tropism, including cytokines and proteins secreted from tissues and tumor cells, the compositions of the immune microenvironment, and oncogenic miRNAs (15). The metabolic preferences of cancer cells may also play a role (16). Tumor cells are long known to exhibit metabolic alterations (17), and reprogrammed metabolism is considered a "hallmark of cancer" (18). Nevertheless, the role of metabolic alterations in metastasis tropism has arguably received less attention.

The MDA-MB-231 cell line was derived from a patient with breast cancer and forms metastases in multiple organs in mice (19–21). The mouse model was used to select *in vivo* for lineages that preferentially home to the bone, brain, or lung (6, 22, 23). The result was a set of parental MDA-MB-231 cells and their matched derivatives, which home to specific organs. A recent study used these cells to find transcriptomic alterations in micrometastases formed in the lung compared with the parental and brain-colonizing cells (24). The study found that mitochondrial electron transport Complex I, oxidative stress, and counteracting antioxidant programs were induced in pulmonary micrometastases, again suggesting a key role for metabolism in the adaptation of cancer cells when colonizing a distant organ. Another study compared the metabolomic profiles of brain- and bone-homing lineages with parental cells (25). The lineages were all cultured in the same *in vitro* conditions, and the comparison revealed differences in intracellular metabolite levels, particularly in purine nucleotides. This study also found increased serine metabolism in all three metastatic lineages (brain, bone, and lung) compared with parental cells, and concluded that these pathways were necessary for metastatic cell growth. However, metabolite levels do not necessarily correlate with metabolic fluxes, and it remains unclear which metabolic functions are selected in organ-specific metastasis.

Here, we used the MDA-MB-231 model to study metabolic fluxes in breast cancer cells with different tropisms. We focused on the brain- (BrM2) and lung-homing (LM2) lineages of MDA-MB-231; the lung and brain have distinct metabolic microenvironments that impose unmistakably different selective pressures (26–30). Our results show that the flux through the glycolytic pathway is increased in brain-homing and especially in lung-homing lineages compared to parental. Importantly, this occurs even though parental cells have higher intracellular levels of glucose and other intermediaries of the glycolysis pathway. We propose that an elevated ratio of lactate dehydrogenase (LDH) to pyruvate dehydrogenase (PDH) gene expression, which indicates a cell state of high glycolytic to lactate flux in LM2 cells, may be a predictor for lung metastasis in patients with breast cancer. Notably, lung metastases in a model of pancreatic cancer had higher lactate production than other metastases did, suggesting that this metabolic trait could be important for lung metastasis in other cancer types.

Materials and Methods

Cell culture

All cell lines were grown in DMEM (Thermo Fisher Scientific, 11965118) supplemented with 10% FBS (made in the MSKCC media core facility) and 1% penn/strep (Thermo Fisher Scientific, 15140122). Cells were grown in a 37°C incubator with humidity and 5% CO_2. Authenticated breast cancer cell lines were obtained from the Massague lab and generated as described previously (6, 22). KPC cell lines were established from pancreatic tumors and its matched metastases in KPC mice, a mouse model of pancreatic cancer described previously (31). The *in vivo* protocols used to generate these cell lines were conducted in accordance with the guidelines of the Institutional Animal Care and Use Committee. Cell line genotypes were confirmed by recombinant genotyping PCR, and cells were passaged at least three times to rule out contamination from normal cells. Cells were confirmed to be *Mycoplasma* free before aliquots were stored at −190°C in low passage numbers.

Cell growth assay

Cell lines were infected with H2B-YFP or H2B-mcherry lentivirus using 20 μg/mL polybrene. After a few days of passage, cells were sorted via FACS. Cells were counted and plated in equal numbers in a 96-well plate, and fluorescent images were taken periodically for several days on a Zeiss microscope. A 5× objective was used in the instrument, and images were either collected once every 24 hours, after which, the plate was returned to the incubator, or once every hour using the custom-made chamber surrounding the microscope that maintained temperature, CO_2, and humidity levels. Images were analyzed using the Zeiss Zen blue software and our own custom-made MATLAB scripts. Data from several independent biological replicates of the growth assay were pooled, and analyzed using a generalized linear mixed-effects regression model with a log function (since the cells are in exponential growth) and random effects for which experiment and well in the plate the data came from. Growth rates were analyzed both for the full data as well as excluding pre-exponential phase growth. For glucose titration: cells were grown in glucose-free media, and full media was titrated and six levels to generate a curve.

Metabolomics

Cells were seeded in T75 flasks, in five replicates per cell line. Two days after plating, cells were trypsinized, counted, and spun down. Media was aspirated from cells, which were then resuspended in PBS and re-spun. PBS was aspirated and the cell pellet was immediately frozen in liquid nitrogen. Samples were shipped to metabolon on dry ice, and metabolite abundance data were normalized to total protein content per sample. Metabolomics analysis: heatmaps, principal component analysis, statistical analysis of abundance fold changes (two-sample *t* test), and partial least squares regression analysis were done in MATLAB using built-in features and custom-made scripts.

RNA expression analysis

mRNA expression data that were published previously (6, 22) were downloaded from Gene Expression Omnibus (accession nos. GSE12237: GSM307534, GSM307535, GSM307536, GSM307578, GSM307579. GSE2603: GSM49953, GSM49954, GSM49955, GSM49956, GSM49957, GSM50017). The Hallmark glycolysis gene set was downloaded from the Gene Set Enrichment Analysis Molecular Signatures Database. Expression fold change relative to parental for each metastatic lineage was calculated for the genes in the Hallmark glycolysis gene set, and a heatmap was generated using MATLAB. The ratio of $(LDHA+LDHB)/(PDHA1+PDHA2+PDHB)$ for each lineage and statistical differences (two-sample *t* test) were calculated in MATLAB.

MITHrIL pathway analysis

The MITHrIL algorithm was used as described previously (32). We used the combined Log2FC values of the differentially expressed genes

(DEG) and altered metabolites identified from BrM2 and LM2 samples. Specifically, the DEGs for BrM2 and LM2 samples were identified from the two public microarray projects used above whereas the altered metabolites were identified from our metabolomics data. Microarray data were first normalized and then the DEGs were identified by using the LIMMA package (Bioconductor; ref. 33). Only the genes with $Log_2FC > 0.6$ or $Log_2FC < -0.6$ with a statistically significant adjusted *P* value (with Benjamini–Hochberg correction) <0.05 were considered differentially expressed and selected for the MITHrIL pathway analysis. The metabolomics data were analyzed using the MetaboDiff package (Bioconductor; ref. 34) and only the metabolites with $Log_2FC > 0.6$ or $Log_2FC < -0.6$ and a statistically significant adjusted *P* value (Benjamini–Hochberg correction) <0.05 were considered as altered metabolites and included in the MITHrIL pathway analysis. All these analyses were performed using the framework Rstudio (R3.5.2). MITHrIL output for the glycolysis/gluconeogenesis pathway was overlaid on the Kyoto Encyclopedia of Genes and Genomes pathway diagram. Total MITHrIL output was imported into MATLAB to generate waterfall plots and clustergrams.

YSI

Cells were cultured in 6-well plates. Eight hours prior to sample collection, media was changed to 2 mL per well, and incubated as above. 1.2 mL were collected from each sample, spun down to remove cell debris, and then frozen until processing by the Cell Metabolism Core Facility. The YSI analyzer in the Cell Metabolism Core Facility detects glucose, lactate, glutamine, and glutamate using immobilized substrate-specific enzymes, which are placed between two selective, interfering membranes. These membranes are coupled to a platinum electrode. The dual-reaction system ultimately detects the rate of electron flow, which is proportional to the metabolite concentration in the sample. Our samples were thawed, plated in a 96-well plate, and inserted into the YSI analyzer machine. Data were normalized to cell count. Statistical analysis of data were done in MATLAB (two-sample *t* test).

Seahorse

A total of 20,000 cells/well were seeded in Seahorse XF plates. The following day, media was changed to the Seahorse XF media with glucose, pyruvate, and glutamine, and standard Seahorse XF protocols were followed. For assessing mitochondrial activity, the Mito Stress Test Kit was used, with 1 μmol/L oligomycin, 1 μmol/L FCCP, and 0.5 μmol/L rotenone+antimycin A. Basal respiration rate corresponded to oxygen consumption excluding nonmitochondrial oxygen consumption (OCR in the presence of rotenone + antimycin A). ATP production corresponded to the difference in basal respiration rate and oxygen consumption in the presence of an ATP synthase inhibitor (oligomycin). For assessing glycolysis, the Glycolytic Rate kit was used, with 0.5 μmol/L rotenone+antimycin A and 50 mmol/L 2-deoxyglucose. Non-CO_2 ECAR was calculated by subtracting mitochondrial OCR*0.6 (standard scaling factor) from the total proton efflux rate. Compensatory glycolysis corresponded to proton efflux rate in the presence of rotenone+antimycin A. For assessing mitochondrial fuel oxidation, the Mito Fuel Flex Test Kit was used with 6 μmol/L BPTES and 4 μmol/L UK5099. Mitochondrial glutamine utilization was calculated by subtracting OCR in the presence of BPTES from total OCR. Mitochondrial pyruvate utilization was calculated by subtracting OCR in the presence of UK5099 from total OCR. All Seahorse data were normalized to cell count, and statistical analyses of fold change differences were done in MATLAB (two-sample *t* test).

Flux balance analysis

A 24-flux metabolic network model that represents glycolysis, reduction of pyruvate to lactate, TCA cycle, glutamine/glutamate metabolism, and oxidative phosphorylation was developed by simplifying the model reported in ref. 35. Experimentally measured glucose uptake, lactate production, glutamine uptake, glutamate production, and oxygen consumption rates (converted to mmol/gDW/hour by assuming averaged cell weight of 1 ng) were used to constrain the corresponding fluxes by setting their lower and upper bounds to the mean measured value minus and plus standard error across all replicates, respectively. Other fluxes were unconstrained with their lower or upper bounds set to −100 or 100, respectively. Considering the flux-balance solutions are not unique, we quantified the uncertainty of unmeasured fluxes by sampling the constrained high-dimensional flux space. Flux sampling allows building marginal distributions of each flux and computing the averaged flux value as the most possible solution under the constraints given by data. For the distribution of flux ratios between metastatic derivatives and parental cell types, we used a bootstrap method to resample the marginal distributions with replacement and calculate the fold change of resampled fluxes. Custom Python codes were developed with the COBRApy package (36) to carry out all metabolic flux modeling and simulations in the paper.

Enzymatic assays

The Hexokinase Activity Assay Kit (Abcam ab136957), Phosphofructokinase Activity Assay Kit (Abcam ab155898), Glyceraldehyde 3 Phosphate Dehydrogenase Activity Assay Kit (Abcam ab204732), Pyruvate Kinase Assay Kit (Abcam ab83432), and Lactate Dehydrogenase Assay Kit (Abcam ab102526) were used and accompanying protocols were followed. Briefly, cells from each lineage were trypsinized, counted, and 250,000 cells were collected for each assay. Cells were washed with PBS, homogenized, and the supernatant was mixed with substrate and probe developer. Absorbance was read at 450 nm, and activity rate was calculated by measuring absorbance at two time points and compared with a standard curve. Negative and positive controls were used.

ELISA assays

The Hexokinase II ELISA Kit (Abcam ab219043), Phosphofructokinase ELISA Kit (MyBioSource MBS163996), Glyceraldehyde-3-Phosphate Dehydrogenase ELISA Kit (MyBioSource MBS701148), Pyruvate Kinase ELISA Kit (Biomatik KC35325), Lactate Dehydrogenase ELISA Kit (ABIN6957356), Pyruvate dehydrogenase (PDH) Profiling ELISA Kit (Abcam ab110174), Pyruvate Dehydrogenase Kinase Isozyme 2 (PDK2) ELISA Kit (MyBioSource MBS108891), and Pyruvate Dehydrogenase Kinase Isozyme 1 ELISA Kit (MyBioSource MBS2885331) were used for protein quantification, and accompanying protocols were followed. The Pierce 660 nm Protein Assay Kit (Thermo Fisher Scientific, 22662) and Pierce Bovine Serum Albumin Standard Pre-Diluted Set (Thermo Fisher Scientific, 23208) were used to normalize to total protein content.

Isotope tracing and GC/MS

Cells were seeded in 6-well plates (300k cells/well, three replicates per condition) in fresh DMEM + 10% dFBS and were refreshed with fresh media 24 hours after seeding. Fourty-eight hours after seeding, the media was exchanged to DMEM + 10% dFBS with ^{12}C glucose or ^{13}C uniformly labeled glucose (CLM-1396, Cambridge Isotopes) for 0, 2, 4, 6, 8 hours. To extract the intracellular metabolites, media was aspirated, 1 mL/well ice-cold 80% methanol was added, and cells were

scraped down. Cells were centrifuged at 20,000 × *g* for 20 minutes at 4°C. The supernatant was collected and dried in a speed vacuum evaporator for 4 to 5 hours. Dried samples were stored in −80°C freezer prior to derivatization. The dried pellets were resuspended in 50 μL methoxyamine (TS-45950, Thermo Fisher Scientific) and shaken at 1,400 rpm at 30°C for 2 hours. 80 μL of MSTFA (TS-48911, Thermo Fisher Scientific) was added to each resuspended pellet and the solution was transferred to autosampler vials with 70 μL of ethyl acetate (1036491000, Merck). Samples were incubated at 37°C for 30 minutes before being run on the GC/MS. The following analytical system was used for metabolomics analysis: Agilent 5977B GC/mass selective detector (MSD) with an Agilent 7890B GC and an Agilent 7693A autosampler. The injection volume was 1 μL. The temperature program was as follows: the initial oven temperature 60°C was held for 1 minute, then programmed to increase at 7.3°C/minute to reach a final temperature of 250°C and held for 10.5 minutes. Helium was used as carrier gas with a constant linear velocity of 1 mL/min. The Agilent metabolite profiling software (MassHunter Qualitative Analysis 10.0 and MassHunter Quantitative Analysis B.08.00), as well as Matlab were used for targeted metabolite identification. Correction for natural isotope abundance was performed using IsoCorrectoR software.

AACR project GENIE analysis

Clinical metadata and genomic data from the metastatic breast cancer cohort within this project was downloaded from the cBio portal (version GENIE 12.0-public). Custom MATLAB scripts were used to calculate the most common metastatic sites and mutations in the selected samples. The MATLAB function fscchi2 was used to determine rank and significance of predictors. General linear regression models were used to determine which predictors were significantly correlated with each metastatic site.

MetMap analysis

Breast cancer cell line metastatic and gene expression data were downloaded from DepMap (https://depmap.org/portal/), a publicaly available cell line information site developed by the Broad Institute. Breast cancer cell lines that had any nonnegative lung tropism were selected. The breast cancer cell line used experimentally in this paper is a triple-negative cell line; restricting the MetMap set to only include triple negative cell lines greatly reduced the number of cell lines and we therefore included all HER2 negative cell lines in our analysis. The ratio of gene expression of (*LDHA*+*LDHB*)/(*PDHA1*+*PDHA2*+*PDHB*) was calculated for each cell line. Cell lines were plotted according to their lung potential and penetrance, as well as LDH/PDH gene expression ratio. Cell lines were grouped as to whether they had >median potential and penetrance or <median. Means between the two groups were compared by a two-sample *t* test. Parallel analysis was done on breast cancer cell lines with any nonnegative brain tropism as a comparison.

Metastatic breast cancer project analysis

The results included here include the use of data from The Metastatic Breast Cancer Project (https://www.mbcproject.org/), a project of Count Me In (https://joincountmein.org/; ref. 37). Clinical metadata, genomic data, and gene expression data for the Metastatic Breast Cancer Project was downloaded from the cBio portal (MBCproject cBioPortal data version March 2020; refs. 38, 39). For generation of these data, tissue biopsies were received as blocks and were not sorted by cell type prior to RNA-seq. Custom MATLAB scripts were used to calculate the most common metastatic sites and mutations in the selected samples. Archetypes were generated by using non-negative matrix factorization, with each sample having probabilistic membership into each archetype. The maximum likelihood archetype was assigned as the given archetype for each sample. Proportions of each metastatic site for each breast cancer mutation, hormone receptor status, and transcriptional archetype were calculated in MATLAB. Patients were then classified according to whether they had metastases to the lung (including patients who had metastases to other sites as well as lung) or metastases to any location other than lung. Data from biopsies that sampled the breast or chest wall were included, whereas the few samples from distal sites were excluded. For patients that had more than one biopsy, the earliest biopsy was used. The ratio of gene expression of (*LDHA*+*LDHB*)/(*PDHA1*+*PDHA2*+*PDHB*) was calculated for each patient; boxplot and statistical analysis of fold change between groups (two-sample *t* test) was done in MATLAB. UMAP (40) analysis of patient archetypes was done in MATLAB after *z*-scoring each sample. The MATLAB function fscchi2 was used to determine rank and significance of predictors. General linear regression models were used to determine which predictors were significantly correlated with each metastatic site. A general linear regression model with LDH/PDH from the primary tumor as the predictor variable and presence or absence of lung metastasis (at any point in time) in the patient as the response variable was analyzed using a ROC curve. LDH/PDH was binarized at its natural inflection point into "high" versus "low" values and used as the sole predictor variable in a prediction model, with presence or absence of lung metastasis as the response. Because there were few patients with lung compared with non-lung metastases, we first randomly selected a subset of non-lung metastatic patients so that there were equal numbers between the two groups and we were adequately powered to test a model. Because of the limited data, we then iteratively left out a single data point, trained the model on the remaining data, and asked the model to predict the presence or absence of lung metastasis in each patient in turn. We then repeated this several times, randomly selecting (with replacement) a subset of non-lung metastatic samples each time. We then calculated the true positive, true negative, false positive, false negative, and overall accuracy from the predictions.

MEMIC assay

Glass coverslips were glued onto glass-bottom dishes (Mattek P06G-1.0–10-F) using Norland optical adhesive 81 such that 1 mm slit of the inner well was uncovered. A handheld UV lamp was held over the plate for 30 seconds to cure the adhesive gel. Wells were filled with sterile water and left under UV in biological hood overnight. Remaining water was aspirated and replaced with media, and incubated overnight at 37°C with humidity and 5% CO_2. Inner wells were plated with cells, and 300 μL media was added to edges of outer wells to prevent evaporation before returning plates to the incubator. After 4 hours, outer wells were filled with 2 mL media. Cells were imaged daily.

Data availability

Metabolomics data generated in this study are publicly available at https://zenodo.org/badge/latestdoi/648288267 (DOI: 10.5281/zenodo.7996343 Release v1.0). Some of the data analyzed in this study were obtained from The Metastatic Breast Cancer Project at https://www.mbcproject.org, and AACR Project GENIE at https://genie.cbioportal.org/login.jsp. Codes and raw data files are available on github: https://github.com/dm2791/A-high-LDH-PDH-ratio-predicts-BC-lung-metastasis. All other raw data are available upon request from the corresponding author.

Results

Clinical characteristics and mutational burden are poor predictors of breast cancer metastatic tropism

We analyzed the metastatic breast cancer cohort within the publicly available cancer registry AACR Project GENIE (41), which includes both mutational and clinical information. The top 5 most common sites of metastasis were liver, lymph node, brain/central nervous system, bone, and lung (Supplementary Fig. S1A, left). Consistent with previous work, each hormone receptor status was distributed across metastatic sites (Supplementary Fig. S1B, top). The most commonly mutated genes, *PIK3CA* and *TP53*, were also present in each of the top 5 metastatic sites, indicating that as expected these oncogenic lesions do not determine metastasis (Supplementary Fig. S1A, right; Supplementary Fig. S1B, bottom). To more rigorously investigate whether clinical characteristics or mutational burden can predict tropism, we used univariate feature ranking for classification and found that the top ranked features associated with tropism were: (i) disease stage at diagnosis, (ii) subtype at diagnosis, and (iii) whether the patient received neoadjuvant or adjuvant trastuzumab therapy (**Fig. 1A**). However, except for trastuzumab treatment correlating with CNS metastases, none of these features significantly correlated with organ-specific metastasis (**Fig. 1B**). It is therefore difficult to use these features as predictors of specific tropism for any given patient. These analyses gave further credence to our hypothesis that additional adaptations—including metabolic alterations—contribute to organ-specific metastasis.

Combined metabolomics and transcriptomics analysis reveals that primary and metastatic lineages have distinct metabolic rewiring

As we found in our analysis of AACR Project GENIE, consistent with epidemiologic data (42), lung and brain are among the most common sites of metastasis in breast cancer. We therefore turned to the MDA-MB-231 breast cancer cell line model and its brain-homing BrM2 lineage and lung-homing LM2 lineage (**Fig. 1C**). Metabolomics profiling revealed that the metabolomes differed for each lineage, indicating that the lines maintain heritable differences in their utilization of metabolic pathways even when they are cultured *ex vivo* in the same condition (**Fig. 1D**). Principal component analysis (PCA) of the metabolite levels showed that the largest differences occur between the parental line and the derived lineages (**Fig. 1E**): all replicates of the parental lineage scored high on PC1, which explained 84% of the variation. A biplot analysis revealed that a single metabolite—glucose—explained a large part of these differences (**Fig. 1E**, shown in gray). In fact, the relative glucose levels in parental cells were >30× higher than in either BrM2 or LM2 cells (**Fig. 1E**, inset). Most other intermediates of glycolysis were also significantly higher in the primary lineage, except for higher 2,3-BPG and pyruvate in BrM2 relative to parental, and higher lactate in LM2 relative to parental (**Fig. 1F**; Supplementary Fig. S1C). Overall, many metabolic alterations from parental to metastasis correlated between BrM2 and LM2 (**Fig. 1G**), and the PCA suggested that the primary metabolic divergence occurred early in the metastatic process with further diversification in the lung and brain: PC2, which explained ∼10% of the variation, distinguished BrM2 from LM2 (**Fig. 1E**). The differences between BrM2 and LM2 occurred mostly in metabolites from amino acid and fatty acid pathways, consistent with prior investigation of brain metastasis (Supplementary Fig. S1D; ref. 43).

Expression of glycolytic pathway genes was also perturbed in the brain- and lung-homing lineages (6, 22). Many of those genes were expressed at lower levels in the metastatic cells compared with parental cells (Supplementary Fig. S1E), confirmed by enrichment of this gene set in parental cells using GSEA (Supplementary Fig. S1F; refs. 44, 45).

A pathway analysis (MITHrIL) integrating the transcriptomic and metabolomic data (Supplementary Fig. S2A; refs. 32, 46) confirmed that glycolysis was among the most significantly perturbed pathways in both metastatic lineages, and that components of glycolysis were largely lower than in parental cells (**Fig. 1H**; Supplementary Fig. S2B). Notably, lactate metabolism was higher compared to parental in LM2 but not BrM2 cells (Supplementary Fig. S2C). Comparing BrM2 to LM2 showed lower levels of brain-associated pathways in LM2, including synapse signaling, and higher oxidative phosphorylation and pyruvate metabolism compared to BrM2 cells, consistent with previous results (Supplementary Fig. S2D; refs. 43, 47).

Glucose flux and lactate secretion increased in metastatic lineages despite lower levels of glycolysis intermediates

The multi-omics analysis revealed differences in the metabolic states of the three lineages. To analyze the differences in cell function, we measured the rate of glucose uptake by the cells in balanced growth using a YSI analyzer. Surprisingly, the glucose influx was not lower but marginally "higher" in the brain-homing lineage and markedly higher in the lung-homing lineage compared to parental (**Fig. 2A**). Lactate secretion was approximately proportionally higher in LM2 cells (**Fig. 2A**).

As measured by a Seahorse XF analyzer, LM2 cells showed the fastest rates of overall extracellular acidification as well as acidification from nonmitochondrial sources (**Fig. 2B** and **C**). Inhibition of the electron transport chain with rotenone and antimycin A further increased extracellular acidification, with LM2 cells again releasing the highest levels of nonmitochondrial acidification among the three lineages (**Fig. 2B**). After this mitochondrial inhibition, adding 2-deoxyglucose halted glycolysis and led to a loss of extracellular acidification, indicating that the increase in acidification was due to compensatory glycolysis in the absence of mitochondrial function (**Fig. 2C**). Furthermore, YSI revealed that both derived lineages consumed slightly less glutamine than parental cells, whereas glutamate secretion remained unchanged (**Fig. 2D**). It is therefore unlikely that glutamine (to pyruvate via the TCA cycle) contributed to the higher rate of lactate production.

We confirmed that mitochondrial function was not impaired in the derived lineages: both lineages had higher mitochondrial respiration rates and ATP-linked respiration (suggesting higher ATP production) compared with the parental line, indicating that the uptake in glucose influx was also not required for glycolysis-derived energy in these cells (Supplementary Fig. S3A and S3B). Overall, the mitochondrial metabolism of LM2 differed the most from that of parental, with BrM2 at an intermediate level (Supplementary Fig. S3C).

Mathematical model and experimental validation explain higher flux despite fewer molecular components

The data presented so far stress an important point: the levels of the metabolic intermediates of a pathway can indicate that a pathway is perturbed, but they do not necessarily correlate with the flux through that pathway. Brain- and lung-homing lineages have higher glucose consumption and lactate production than the parental lineage despite lower levels of the molecular components—intermediary metabolites and even the mRNAs of pathway enzymes—of the glycolytic pathway. These differences were marginal in brain-homing cells and robust in lung-homing cells. To understand this apparent contradiction, we

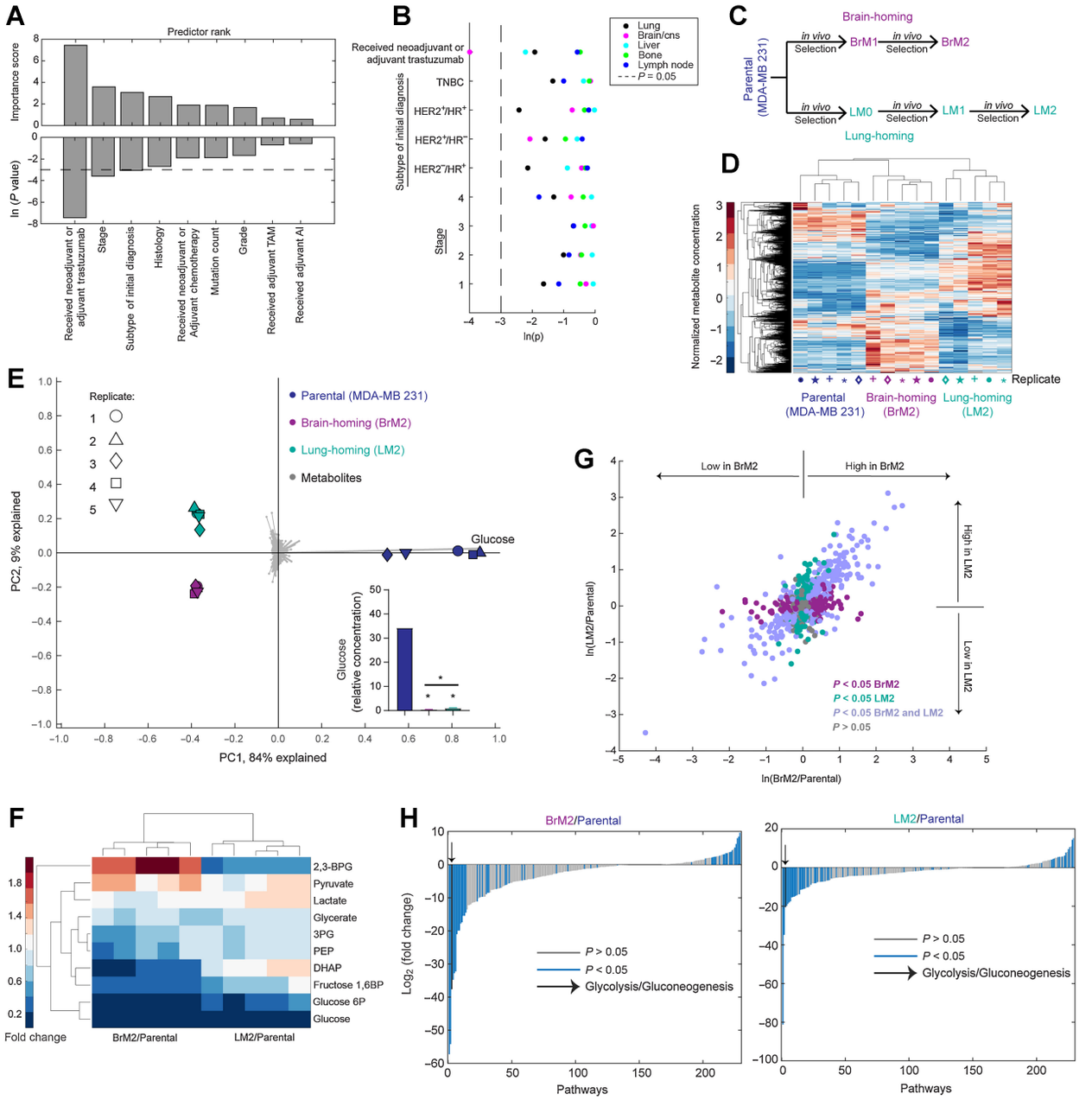

Figure 1.

Divergent metastatic lineages maintain heritable differences from their parental lineage *ex vivo*. Integrated metabolomics and transcriptomics show differences in glycolysis pathway in primary versus metastatic lineages. **A,** Feature selection analysis of AACR Project GENIE database: predictor rank and *P* value of clinical traits and mutational burden. Three features passed a *P* value of <0.05. **B,** Individual linear regression models using the significant features from **A** for each of the top 5 metastatic sites (lung, $n = 26$; brain, $n = 32$; liver, $n = 60$; bone, $n = 26$; lymph node, $n = 51$). Receiving trastuzumab correlated with brain/CNS metastases; no other features significantly correlated with any of these metastatic sites. **C,** Diagram of the *in vivo* selection, which started with the parental lineage MDA-MB-231 and led to brain-homing BrM2 and lung-homing LM2 derivatives. **D,** Heatmap of metabolite levels of parental and metastatic derivatives. Each cell line had five replicates that clustered together. **E,** PCA of parental, BrM2, and LM2 metabolite levels, overlaid with a biplot (gray) showing the correlations of individual metabolites. The spoke corresponding to glucose strongly associates with PC1. Inset, bar plot of glucose levels: fold-change relative to parental: BrM2: 73-fold, $P = 0.0004$; LM2: 33-fold, $P = 0.001$. Fold change LM2/BrM2: 2-fold, $P = 0.000007$. *, $P < 0.05$ compared with parental. *, $P < 0.05$ between BrM2 and LM2. No asterisk, $P > 0.05$. Data are represented as mean ± SD. **F,** Heatmap of the glycolysis pathway metabolites, showing BrM2 versus parental and LM2 versus parental. **G,** Scatterplot of ln(fold change) of metabolite levels in derivative lineages versus parental. Dots are colored according to significance. **H,** Waterfall plot of MITHrIL output comparing BrM2 with parental networks, highlighting the glycolysis/gluconeogenesis pathway (left). Waterfall plot of MITHrIL output comparing LM2 with parental networks, highlighting the glycolysis/gluconeogenesis pathway (right). See also Figs. S1 and S2.

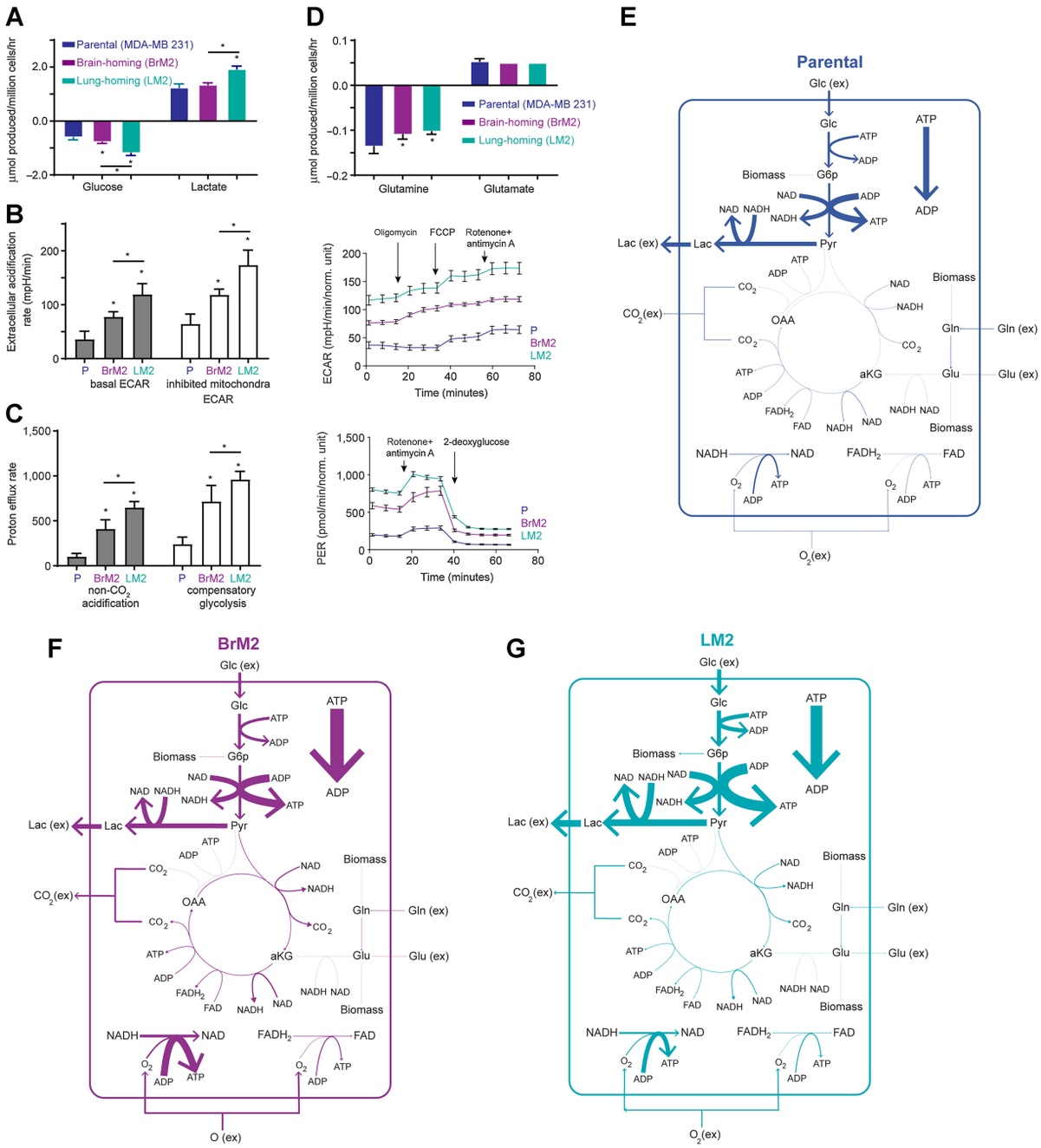

Figure 2.

Glucose uptake and lactate secretion increased in metastatic lineages. Mathematical model predicts higher glycolytic flux despite lower levels of glycolysis intermediates. **A,** YSI analysis of glucose uptake and lactate production. Glucose fold-change relative to parental: BrM2: 1.3-fold, $P = 0.04$; LM2: 2.0-fold, $P = 0.001$. Fold change LM2/BrM2: 1.5-fold; $P = 0.002$. Lactate fold change relative to parental: BrM2: 1.1-fold, $P = 0.30$; LM2: 1.6-fold, $P = 0.002$. Fold change LM2/BrM2: 1.4-fold, $P = 0.001$. **B,** Seahorse analysis of basal ECAR as well as ECAR after mitochondrial inhibition by antimycin A and rotenone. Extracellular acidification rate (right) and quantification (left). Basal ECAR fold change relative to parental: BrM2: 2.2-fold, $P = 0.00002$; LM2: 3.3-fold, $P = 0.0000004$. Fold change LM2/BrM2: 1.5-fold, $P = 0.0003$. Mitochondrial-inhibited fold change relative to parental: BrM2: 1.8-fold, $P = 0.000009$; LM2: 2.7-fold, $P = 0.0000005$. Fold change LM2/BrM2: 1.5-fold, $P = 0.0002$. **C,** Seahorse analysis of nonmitochondrial ECAR and compensatory glycolysis. Proton efflux rate (right); quantification (left). Nonmitochondrial ECAR fold change relative to parental: BrM2: 3.1-fold, $P = 2 \times 10^{-20}$; LM2: 4.5-fold, $P = 9 \times 10^{-36}$. Fold change LM2/BrM2: 1.4-fold, $P = 8 \times 10^{-12}$. Compensatory glycolysis fold change relative to parental: BrM2: 2.6-fold, $P = 4 \times 10^{-16}$, LM2: 3.4-fold, $P = 1 \times 10^{-31}$. Fold change LM2/BrM2: 1.3-fold, $P = 1 \times 10^{-8}$. **D,** YSI analysis of glutamine uptake and glutamate production. Glutamine fold change relative to parental: BrM2: 0.8-fold, $P = 0.005$; LM2: 0.8-fold, $P = 0.001$. Fold change LM2/BrM2: 0.9-fold, $P = 0.6$. Glutamate fold-change relative to parental: BrM2: 0.9-fold, $P = 0.9$; LM2: 0.9-fold, $P = 0.9$. Fold change LM2/BrM2: 1-fold, $P = 1$. For **A** to **D**, *, $P < 0.05$ compared with parental. *, $P < 0.05$ between BrM2 and LM2. No asterisk, $P > 0.05$. Data are represented as mean ± SD. **E–G,** Mathematical modeling of fluxes of select metabolic pathways for parental, BrM2, and LM2 lineages, respectively. Data from **Fig. 2** and Supplementary Fig. S3 were used to constrain the model, and values for unknown fluxes were calculated. Fluxes are represented as most likely values. See also Supplementary Fig. S3.

turned to a systems level investigation using flux balance analysis (FBA), a mathematical method to assess utilization of metabolic pathways in a network. We adapted a model of the flux rates in cancer cell metabolism (35)—a 24-flux metabolic network model—and ran simulations constrained by the external fluxes measured by YSI or Seahorse XF while unknown internal fluxes were unconstrained. Given that the flux-balance solutions were not unique, we quantified the uncertainty of unmeasured fluxes by sampling the constrained high-dimensional flux space. Flux sampling allowed us to compute the most likely solution under the constraints given by data. Our model would therefore help distinguish between two competing hypotheses: (i) that lactate production and glycolysis were uncoupled in LM2 cells, with elevated glucose uptake redirected to a different pathway and lactate production coming from other sources, or (ii) that glycolytic flux was indeed high in LM2 cells and that the molecular components of the pathway were truly anticorrelated with the flux.

The model predicted that glycolytic flux should indeed be the highest in LM2 cells and lowest in parental cells (**Fig. 2E–G**; Supplementary Fig. S3D–S3F). To experimentally validate that LM2 cells have higher glycolytic flux, we traced ^{13}C-labeled glucose and found that the turnover of glucose-derived lactate was highest in LM2 cells (**Fig. 3A**; Supplementary Fig. S4A and S4B). Furthermore, we directly tested the enzymatic activity of four key steps in glycolysis as well as lactate dehydrogenase activity. LM2 cells had the highest levels of activity while parental cells had the lowest levels (**Fig. 3B–F**). Protein levels of enzymes in early glycolysis also did not correlate with flux; however, there were significant increases in pyruvate kinase and lactate dehydrogenase B protein levels in LM2 cells, suggesting that these enzymes may contribute to driving the overall increase in flux through the pathway (Supplementary Fig. S4C–S4H).

Interestingly, the model indicated that the two metastatic lineages can divergently modulate how nutrients are used. For example, unlike LM2 cells, flux from pyruvate to lactate was calculated to be approximately equal in parental and BrM2 cells, despite the higher glucose uptake in BrM2 compared with parental. The FBA showed that BrM2 cells used these excess glucose-derived carbons to fuel the TCA cycle while lowering the use of glutamine compared with parental cells, allowing BrM2 cells to "catch up" to the level of ATP production in LM2 cells despite lower glucose uptake than LM2 (Supplementary Fig. S3D). These model predictions were confirmed by additional Seahorse measurements, showing that mitochondrial pyruvate utilization was higher in metastatic lineages compared with parental cells and mitochondrial glutamate utilization was lower in metastatic lineages compared to parental cells (Supplementary Fig. S4I and S4J).

A high LDH/PDH ratio supports constitutive lactate production in lung metastases

Although the results of our flux-balance model predicted perhaps the most straightforward solution, we wanted to understand the biochemistry of how glycolytic flux can be high in LM2 cells despite low levels of glycolysis metabolites: glycolysis is inhibited by its products (48), and therefore low levels of metabolic intermediates will prevent feedback inhibition and support a high flux. This can be achieved by sustaining flow into a "sink": for example, lactate efflux. Therefore, although an apparent paradox, the lower levels of glycolytic intermediates in LM2 cells relative to parental are not in conflict with higher flux and may be required to maintain high glycolysis flux in the absence of any other regulation. Pyruvate—the end product of glycolysis—can be converted either to lactate or to acetyl-coA. However, increased flux into acetyl-coA and subsequent mitochondrial activity increases ATP, and a high ATP/AMP ratio also allosterically inhibits enzymes in glycolysis (48). Therefore, directing pyruvate predominately to lactate rather than acetyl-coA would better serve to maintain a high glycolytic flux. Indeed, our model predicts that although some of the increased pyruvate in LM2 cells is directed to mitochondrial utilization, the majority is directed to lactate (Supplementary Fig. S3F).

To determine whether this was indeed the case in our cell lines, we compared flux rates from glucose into either lactate or TCA cycle intermediates. ^{13}C glucose tracing showed that the rate of glucose-derived flux from pyruvate into lactate is higher than the rate of flux from pyruvate into citrate in LM2 cells but not in parental or BrM2 cells (**Fig. 3G**; Supplementary Fig. S4K and S4L). The ratio of slopes of lactate to citrate labeling was accordingly higher in LM2 cells compared with the other lineages (**Fig. 3H**). Because ^{13}C labeling plateaued after 2 hours, we also compared the ratios of ^{13}C lactate to citrate levels at 2 hours of tracing, and confirmed that LM2 cells had the highest ^{13}C lactate/^{13}C citrate ratio (Supplementary Fig. S4M). Pyruvate dehydrogenase (PDH) protein levels were lowest in LM2 cells (**Fig. 3I**) whereas PDK protein levels were unchanged, indicating that regulation of PDH activity is unlikely to be posttranslational (Supplementary Fig. S4N and S4O). Together, these data indicate that the LDH–PDH fulcrum associates with lactate production and overall glycolytic flux.

Interestingly, expression of glucose transporter *SLC2A1* was higher in LM2 compared with parental, whereas there was no change in glucose transporter expression in BrM2 cells (Supplementary Fig. S4P and S4Q). These suggest that although LM2 cells achieve high glucose uptake and glycolytic flux by increasing the total number of pathway channels, BrM2 cells marginally increase glycolytic flux compared with parental cells by increasing turnover downstream.

Directly measuring metabolic flux can be challenging in a clinical setting. We therefore hypothesized that although flux does not correlate with metabolic gene expression in a linear pathway, ratios of metabolic transcripts may better indicate cell function. Consistent with our above findings, LM2 cells had a significantly higher ratio of LDH/PDH gene expression than both parental and BrM2 lineages, largely driven by the change in *LDHB* (**Fig. 3J**; Supplementary Fig. S4R).

We were curious as to whether breast cancer cell lines, which have the capability to form lung metastasis, have higher LDH/PDH gene expression than non-lung metastatic breast cancer cell lines. To assess this, we used data from the Broad Institute's MetMap, which determined the potential and penetrance of various organ metastases in multiple cell lines, and transcriptomic data of these cell lines from DepMap (49–51). We find that breast cancer cell lines with high LDH/PDH also had higher lung metastatic potential and penetrance (**Fig. 3K** and **L**), including MDA-MB-231 cells. This correlation did not hold true for brain metastasis (Supplementary Fig. S4S and S4T). We hypothesize that high LDH/PDH expression in the primary breast tumor is indicative of future lung metastases, where the value may be even more exacerbated (as we see in our LM2 lineage).

Clinical data show that LDH/PDH gene expression signature is higher in breast cancers that metastasize to the lung

To test the clinical relevance of our findings, we asked whether the ratio of LDH/PDH expression was higher in the primary tumors of patients who developed lung metastasis. We analyzed the Metastatic Breast Cancer Project dataset (37), which includes a diverse cohort of >100 patients with metastases in multiple sites and has not only clinical and mutational information but also transcriptional data. The most common metastatic sites and top mutations in this cohort matched those in the AACR Project GENIE cohort, indicating that both are good representatives of the population (Supplementary Fig. S5A and S5B). As with project GENIE, neither hormone receptor status nor

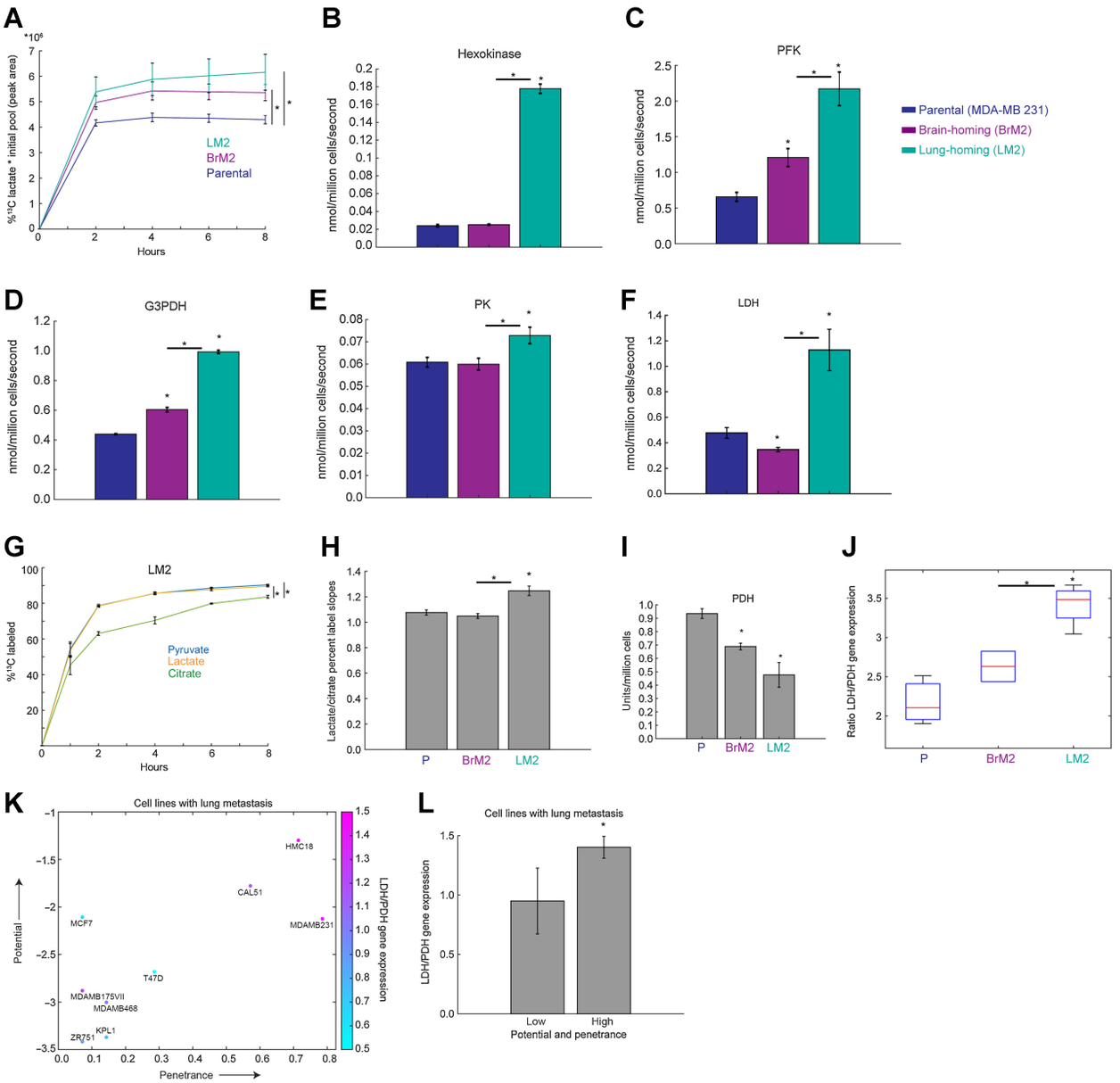

Figure 3.

Experimental validation confirms higher glycolytic flux and identifies that a high ratio of LDH/PDH associates with constitutive lactate efflux in LM2 cells. **A,** Glucose-derived lactate turnover measured by ^{13}C glucose tracing over 8 hours. One-way ANOVA parental versus BrM2 $P = 0.005$; parental versus LM2 $P = 0.007$; LM2/BrM2: $P = 0.06$. **B,** Enzymatic activity of hexokinase. Fold change relative to parental: BrM2: 1.1-fold, $P = 0.4$; LM2: 7.4-fold, $P = 0.00007$. Fold change LM2/BrM2: 7.0-fold, $P = 0.00006$. **C,** Enzymatic activity of phosphofructokinase. Fold change relative to parental: BrM2: 1.8-fold, $P = 0.003$; LM2: 3.3-fold, $P = 0.003$. Fold change LM2/BrM2: 1.7-fold, $P = 0.004$. **D,** Enzymatic activity of glyceraldehyde 3-phosphate dehydrogenase. Fold change relative to parental: BrM2: 1.4-fold, $P = 0.002$; LM2: 2.3-fold, $P = 0.00001$. Fold change LM2/BrM2: 1.6-fold, $P = 0.00003$. **E,** Enzymatic activity of pyruvate kinase. Fold change relative to parental: BrM2: 0.98-fold, $P = 0.08$; LM2: 1.2-fold, $P = 0.04$. Fold change LM2/BrM2: 1.2-fold, $P = 0.03$. **F,** Enzymatic activity of lactate dehydrogenase. Fold change relative to parental: BrM2: 0.7-fold, $P = 0.007$; LM2: 2.4-fold, $P = 0.003$. Fold change LM2/BrM2: 3.2-fold, $P = 0.001$. **G,** Percentage of ^{13}C-labeled lactate, citrate, and pyruvate in LM2 cells. One-way ANOVA pyruvate/citrate $P = 0.002$; pyruvate/lactate $P = 1$; citrate/lactate: $P = 0.003$. **H,** Relative rates of lactate versus citrate ^{13}C labeling. P value parental versus BrM2 $P = 0.16$, parental versus LM2 $P = 0.002$, BrM2 versus LM2: $P = 0.001$. **I,** Protein quantification of pyruvate dehydrogenase. Fold change relative to parental: BrM2: 0.7-fold, $P = 0.001$; LM2: 0.5-fold, $P = 0.02$. Fold change LM2/BrM2: 0.7-fold, $P = 0.08$. For **A** to **I**, data are represented as mean ± SD. **J,** Boxplot of LDH/PDH gene expression ratio in all three lineages. Fold change relative to parental: BrM2: 1.2-fold, $P = 0.2$; LM2: 1.5-fold, $P = 0.007$. Fold change LM2/BrM2: 1.3-fold, $P = 0.03$. Data represented as mean ± IQR. For all bar and boxplots, *, $P < 0.05$ compared with parental. *, $P < 0.05$ between BrM2 and LM2. No asterisk, $P > 0.05$. **K,** Scatter plot of HER2-negative breast cancer cell lines that had lung metastasis in MetMap: lung metastatic penetrance versus potential. Cell lines are colored by their respective LDH/PDH gene expression ratio. **L,** Cell lines were grouped into those that had greater than median penetrance and potential, or less than median. Quantification of LDH/PDH in these two groups, $P = 0.03$. See also Supplementary Fig. S4.

oncogenic lesions correlated with organ site in the MBCP cohort (Supplementary Fig. S5C and S5D). To determine whether metastatic site correlated with transcriptomic state, we used nonnegative matrix factorization to generate six archetypes from transcriptomics, and clustered the samples using UMAP analysis (Supplementary Fig. S5E). The top metastatic sites span several archetypes, indicating—also as expected—that general transcriptomic signatures do not strongly correlate with tropism (Supplementary Fig. S5F).

We then asked whether differences in the LDH/PDH ratio in the primary tumor could predict tropism. We restricted the cohort to patients whose biopsies were from the breast or chest wall, excluding patients whose biopsies were only taken from distal sites. We then classified patients according to whether they developed a lung metastasis, brain metastasis, or any metastasis other than to the lung or brain throughout the course of their cancer progression. Patients with lung metastasis had a higher LDH/PDH expression ratio in their breast biopsy than patients with other metastases, supporting our hypothesis that a high ratio in the primary tumor is characteristic of future lung metastasis (**Fig. 4A**). Patients with brain metastases did not have a higher LDH/PDH ratio than those with other metastases. The high LDH/PDH ratio in patients with lung metastases did not necessarily correlate with high LDH expression (Supplementary Fig. S5G), and there were no significant differences in the expression of LDH nor PDH genes between patients with lung, brain, or other metastases (Supplementary Fig. S5H). This supports our *in vitro* results that the ratio between the two transcripts is a better indicator of cell function. Similar to our *in vitro* results, *SLC2A1* expression trended higher in patients with lung metastasis (Supplementary Fig. S5I). Lung metastases did not cluster by archetypes identified by gene expression (**Fig. 4B**). Interestingly, the magnitude of the LDH/PDH ratio in patient samples also did not cluster by archetype, indicating that the LDH/PDH ratio is independent of the major transcriptomic cell state in this breast cancer cohort (**Fig. 4C**). To see which features could be predictors of tropism, we performed univariate feature ranking for classification. The LDH/PDH ratio was the top ranked and only significant feature among those tested, outranking general transcriptomic archetype, mutational burden, and clinical traits (tumor stage and subtype; **Fig. 4D**). General linear regression models selected the LDH/PDH ratio as a significant correlate of lung metastasis but not metastases to other organs (**Fig. 4E**). Neither *LDHA*, *LDHB*, *PDHA1*, *PDHA2*, nor *PDHB* individually were significantly correlated with tropism (**Fig. 4D**), suggesting that the ratio of LDH/PDH expression in particular is a potential marker of breast cancer metastasis to the lung.

To test the predictive capability of LDH/PDH for lung metastasis, we fit a general linear regression model with LDH/PDH from the primary tumor as the predictor variable and presence or absence of lung metastasis (at any point in time) in the patient as the response variable. The area under the ROC curve was 0.78, suggesting a strong correlation (**Fig. 4F**). We then binarized LDH/PDH as either "high" or "low" based on its natural inflection point in our data (Supplementary Fig. S5J) and trained a model on a subset of the data. We asked the model to predict lung metastasis in test data, with only LDH/PDH as the predictor. The LDH/PDH classification alone predicted the presence or absence of lung metastasis with an overall accuracy of 74% (**Fig. 4G**).

Lactate efflux may be a convergent trait in lung metastases

Although the parental MDA-MB-231 lineage already has increased aerobic glycolysis compared with noncancerous cells, our observations suggest the lung-homing lineage has an even more augmented Warburg effect, the most prevalent purpose of which is thought to be for enhanced anabolism (52). Despite these differences, all three lineages grew at similar rates, suggesting that the metabolic adaptation we observed served a different purpose than faster biomass production (**Fig. 5A**; Supplementary Fig. S6A). When we considered only cells in the exponential phase of growth and excluded the initial lag-phase, the brain- and lung-homing lineages grew slightly faster than the parental lineage. These suggests that established metastatic tumors may mildly outpace primary tumor cells in growth rate. However, the marginal increase in exponential-phase growth rate was smaller than the magnitude of metabolic changes observed above, supporting the notion that the faster influx of glucose serves another function (53).

Despite different glucose uptake rates, BrM2 and LM2 cells were equally sensitive to glucose deprivation (Supplementary Fig. S6B). We hypothesized that increased acidification of the microenvironment may give LM2 cells a selective advantage in certain environments. Indeed, BrM2 cells were more susceptible to growth inhibition by low levels of exogenous lactate than LM2 cells were (**Fig. 5B**).

To understand how this would affect growth in a spatially-structured tumor, we employed the metabolic microenvironment chamber (MEMIC): in this system, cultured cells are covered by a glass plate such that only one edge of the well is exposed to media and oxygen, forming a directional gradient of diffusible molecules consumed or produced by the cells (54). This formation of self-generated metabolic gradients of nutrients and waste mimics the natural gradients found in a solid tumor. As expected, BrM2 cells grew more poorly farther along the gradient, in regions with poor perfusion (**Fig. 5C**; Supplementary Fig. S6C and S6D). However, LM2 cells were mostly unaffected by the gradient (**Fig. 5C**; Supplementary Fig. S6C and S6D). Taken together, our results suggest that LM2 cells produce more lactate than BrM2 cells do and are not inhibited by an acidic microenvironment, leading to an advantage over BrM2 cells in certain environments.

To see if enhanced lactate production could be a feature of lung metastasis in other cancer types, we measured fluxes in a $Kras^{G12D/+}$; $p53^{R172H/+}$ pancreatic cancer model with lineages that metastasize to the liver and lung (31). As with our breast cancer model, the three lineages had distinct metabolomes (Supplementary Fig. S6E). Compared with both parental pancreatic cells and liver-homing metastases, lung-homing metastases had higher lactate efflux and extracellular acidification (**Fig. 5D** and **E**; Supplementary Fig. S6F–S6I). Lung-homing cells in this model trended toward higher glucose uptake than the other lineages (**Fig. 5D**). ^{13}C glucose tracing shows that lung-homing cells had higher lactate turnover and glucose-derived ^{13}C lactate than the other two lineages did (**Fig. 5F**; Supplementary Fig. S6J). However, lung-homing cells in the pancreatic cancer model did not have a higher LDH/PDH gene expression ratio compared with parental cells, and significantly but only modestly higher LDH protein levels and modestly lower PDH protein levels compared with the other lineages (Supplementary Fig. S6K–S6M). Nonetheless, LDH enzymatic activity was markedly higher in the lung-homing lineage compared with parental and liver-homing cells (**Fig. 5G**). Our results indicate that lactate output may be a conserved feature in lung metastasis across more than one cancer type, but that different molecular mechanisms can be associated with this trait in different cancers.

Discussion

Our results produced five biological insights: first, levels of mRNAs and metabolic intermediates may anticorrelate with flux. Second, different lineages evolved from the same line can have distinct heritable metabolic fluxes that persist even when cultured in the same conditions

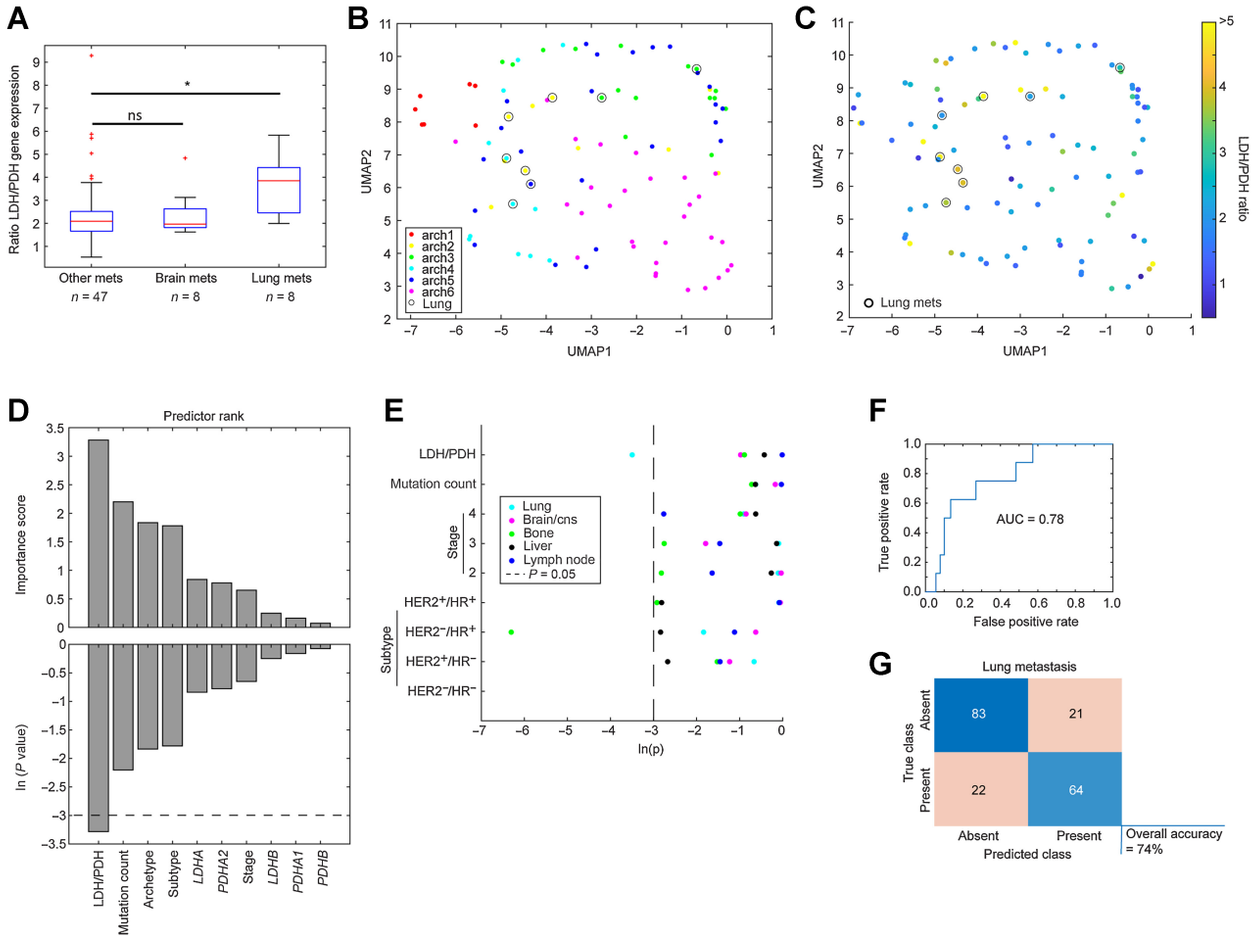

Figure 4.

A high LDH/PDH ratio predicts lung metastases in clinical breast cancer database. **A,** Boxplot of ratio of LDH gene expression to PDH gene expression in patients' primary tumors from The Metastatic Breast Cancer Project. The "Lung" classification includes patients who had lung metastases, "Brain" classification includes patients who had brain/CNS metastases, and "Other" classification includes patients who had metastases other than to the lung or brain/CNS at any point in time. Brain/other, $P = 0.9$; lung/other, $P = 0.04$; lung/brain, $P = 0.057$. Data represented as mean ± IQR. **B,** UMAP of transcriptomics of MBCP patients, colored by archetype. Transcriptomes of patients who developed lung metastasis are circled. **C,** UMAP of transcriptomics of MBCP patients, colored by LDH/PDH ratio. Patients with lung metastases are circled. **D,** Feature selection analysis of MBCP database: predictor rank and *P* value of clinical traits and mutational burden. Only one feature (LDH/PDH expression) passed a *P* value of <0.05. **E,** Individual linear regression models (lung, $n = 8$; brain, $n = 8$; liver, $n = 25$; bone, $n = 46$; lymph node, $n = 15$. Note that these are not mutually exclusive; some patients had more than one of these metastases.) Because there was only one significant feature identified in **D**, we also included the second ranked feature (mutation count). Because subtype and stage were significant features selected in **Fig. 1**, they were also included in our model here. The LDH/PDH ratio correlated with lung but not other metastases. **F,** ROC curve of general linear regression model, with LDH/PDH ratio as predictor variable and presence or absence of lung metastasis as response variable. **G,** Confusion matrix of model prediction, with absolute numbers of true positive, true negative, false positive, and false negatives, as well as overall percent accuracy in predicting presence or absence of lung metastasis using only binarized LDH/PDH as a predictor. *, $P < 0.05$; ns, nonsignificant. Data represented as mean ± SD. See also Supplementary Fig. S5.

ex vivo. These suggest that these metabolic adaptations in these lineages are likely selected in different tissues, rather than plastically changing in different environments. In our case, lung-homing cells exhibited by far the greatest glucose uptake and lactate production despite low levels of glycolytic intermediates. Third, this apparent paradox can be reconciled if feedback inhibition of the glycolysis pathway is prevented, a finding we modeled with flux-balance analysis and confirmed by ^{13}C glucose tracing and measuring glycolytic enzymatic activities directly. Fourth, this distinct metabolic behavior in lung-homing cells was characterized by a high LDH/PDH ratio, which also predicted lung metastasis in patients with breast cancer. Fifth, this metabolic effect was also present in pancreatic cancer lung (but not liver) metastasis. We can speculate that lactate production itself may be a convergent evolutionary step for lung metastasis in some cancers.

Gene signatures are typically sets of expression changes that may be independent of each other. Our results support gene signatures that are more complex (55): the LDH/PDH expression ratio may be more important to maintain a high glycolytic flux in breast cancer rather than the expression of either gene or both genes if their ratio does not change (56). Interestingly, a mouse model of breast cancer metastasis found that metastatic cells can upregulate both glucose consumption/lactate production and oxidative phosphorylation compared with parental cells, consistent with our results, but that liver metastases

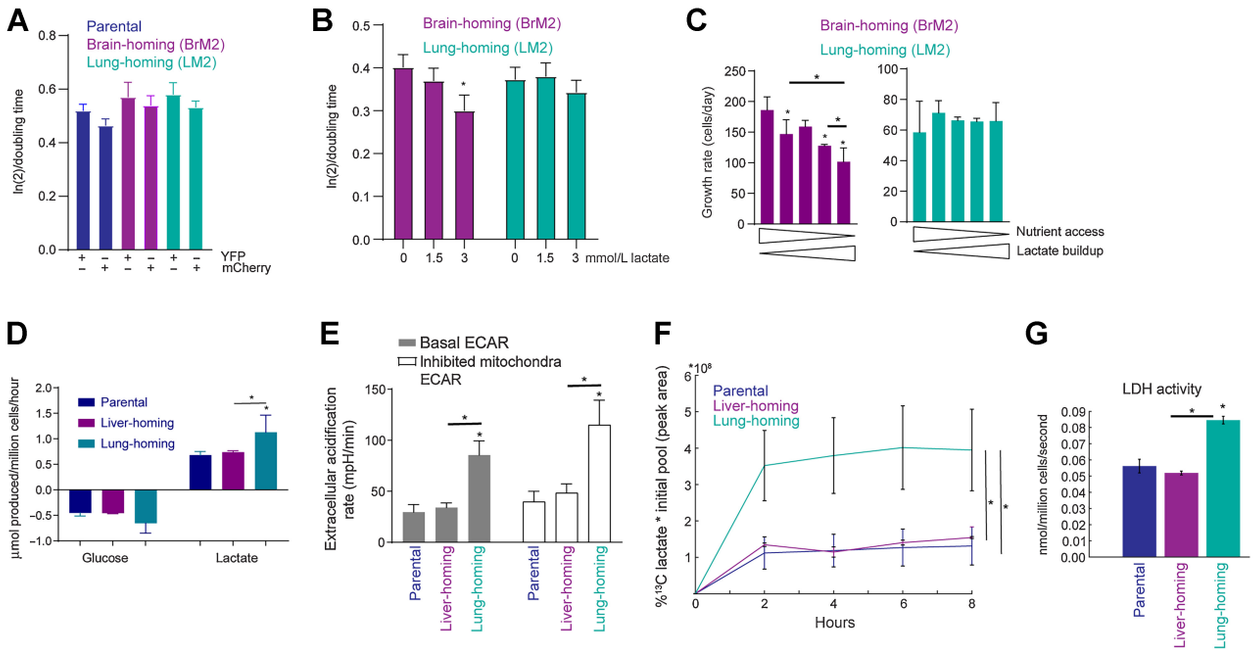

Figure 5.

Lactate efflux in lung metastases may be a convergent trait across cancer types. **A,** Growth rates of parental, BrM2, and LM2 lineages. Cell label (YFP or mCherry) does not affect growth rate. $P > 0.05$ for all comparisons. **B,** Growth rates of BrM2 and LM2 cells with exogenous lactate. **C,** Growth rates of BrM2 (left) and LM2 (right) in MEMIC chambers, cells labeled with YFP. For **B** and **C,** *, $P < 0.05$ compared with first bar in each panel. *, $P < 0.05$ between other groups. No asterisk, $P > 0.05$. **D,** YSI analysis of glucose uptake and lactate efflux in pancreatic cancer cell lines: parental, liver-homing metastatic lineage, lung-homing metastatic lineage. Glucose parental versus lung-homing $P = 0.09$. Lactate parental versus lung-homing $P = 0.006$, liver-homing versus lung-homing $P = 0.02$. **E,** Seahorse analysis of basal ECAR as well as ECAR after mitochondrial inhibition by antimycin A and rotenone in pancreatic cancer cell lines. For **D** to **E**, *, $P < 0.05$ compared with parental. *, $P < 0.05$ between liver- and lung-homing. No asterisk, $P > 0.05$. **F,** Glucose-derived lactate turnover measured by ^{13}C glucose tracing over 8 hours. One-way ANOVA parental versus liver-homing $P = 0.06$, parental versus lung-homing $P = 0.045$, liver-homing versus lung-homing $P = 0.039$. **G,** Enzymatic activity of lactate dehydrogenase. Lung-homing relative to parental: $P = 0.0005$, lung-homing relative to liver-homing: $P = 0.0003$. *, $P < 0.05$ compared with parental. *, $P < 0.05$ between liver- and lung-homing. No asterisk, $P > 0.05$. Data represented as mean ± SD. See also Supplementary Fig. S6.

regulate the balance between the two in a HIF-1α and PDK1-dependent manner (16). These support our idea that metabolic balance is more complex than the expression of genes taken independently, and that expression in the context of other genes *and environmental cues is important. Although lactate production coincided with reduced mitochondrial metabolism in liver metastasis (16), lung metastasis in our model increased both glucose-derived lactate and TCA cycle intermediates, but increased lactate proportionally more. In addition, LDH/PDH is not associated with liver metastasis in our patient analysis, suggesting that different molecular mechanisms in liver versus lung metastasis lead to a similar metabolic output.

The lung and brain are organs with very different metabolic microenvironments, which may impose different selective pressures on disseminated breast cancer cells. Our MEMIC data show that lung- and brain-homing lineages could be selected differently depending on the metabolic microenvironment. It remains an open question why certain environments are favored, but there are several possibilities:

Metastatic cells have been shown to have intermediate gene expression signatures that reflect both primary tumors from their tissue of origin and primary tumors from their disseminated site. In triple-negative breast cancer, metastatic cells were more similar to primary tumors from their destination site (43). Lung cells and lung tumors can oxidize lactate as a fuel (29, 30, 57), and it is therefore possible that metastatic cells that colonize the lung are selected for their lactate production as a carbon source for the organ tissue or mimic features of lung cancers that augment their ability to form macrometastases. Secreted lactate can also lower the pH of the microenvironment and may trigger tissue-repair responses in stromal cells that help tumor development (58). Lactate has been shown to increase migration and metastases by degrading the extracellular matrix (59).

Interestingly, exogenous lactate decreases glucose utilization in the lung (60). This may increase glucose availability for colonizing cells, leading to a feed-forward loop in lung metastases. Consistent with our results, previous work found that pancreatic cancer cells that undergo the epithelial–mesenchymal transition increase lactate output (61). Lung tissues may select for metastases with the highest lactate production regardless of their cell of origin.

On the other hand, the central carbon metabolic alterations in brain-homing cells compared to parental cells were modest, especially when contrasted with the strong alterations we saw in lung-homing cells. This could indicate that the selection for metabolic adaptation was stronger in the lung. However, it could also indicate that all metastatic cells originally carried the adaptations found in LM2, but that the BrM2 lineage, in the process of overcoming additional challenges like crossing the blood–brain barrier, lost some of these metabolic alterations in favor of other, more necessary, adaptations to the brain microenvironment. BrM2 cells only exhibited marginally higher glucose uptake relative to parental cells, and previous work showed that breast cancer brain metastases proliferated in the absence of glucose by catabolizing amino acids for gluconeogenesis (47). It is possible that the metabolic composition of

the brain, an organ that consumes glucose at high rates, imposes selection for cells that avoid competing with brain cells for this resource (62).

The diverse metabolic changes we observed in the three lineages suggest that a primary tumor induced by a set of driver genes can still have underlying diversity at the metabolic level, driven by nondriver genetic differences. This would reinforce that metabolic rewiring in cancer cells is more complex than single oncogenic changes (63). However, we cannot rule out the possibility that the cells in the primary lineage that ultimately produced BrM2 and LM2 had mutations in driver genes that the rest of the primary lineage did not share, and were undetected in the primary tumor due to low abundance. Another possibility is that alterations in common driver genes occur at the transcript, rather than genomic level, in metastatic lineages. A study in MDA-MB-231 cell lines found c-myc overexpression in metastases, especially in the bone-homing lineage (25). Disseminated cells may also be plastic due to reversible epigenetic states that can be reprogrammed depending on the distal tissue (64).

Perhaps most importantly, our work warns that metabolomic profiling alone—or even in combination with transcriptomic profiling—may help identify alterations in metabolic pathways but may not suffice to show how cells use their metabolic fluxes. The static pictures provided by metabolomics and transcriptomics may require a combination of flux measurements and mathematical models to show how cells rewire metabolism. A recent study found that oxidative phosphorylation metabolites and transcripts were increased in micrometastases compared with primary tumor cells, and inhibition of that pathway reduced lung metastases in mouse models (65). Although this seems to contrast with our data, the study is consistent with both ours and others' findings that metastatic cells in general increase bioenergetics. Although important for early steps in the metastatic cascade, our results would indicate that established macrometastases in the lung carry adaptations that include an enhanced Warburg effect.

We focused on fluxes through central carbon metabolism, but we acknowledge that the metastatic process, including organ-specific metastasis, likely involves many other secreted and consumed metabolites, and we did not directly measure the flux for all relevant compounds (66). We also do not yet know whether the metabolic changes we identified were the cause of lung- or brain-specific metastasis or a byproduct of the selection at the distal organ, a question we will explore in future studies. Together, our *in vitro*, *in silico*, and clinical data analyses highlight that metabolism—currency of all physiologic processes—plays an essential role in the connection from gene to phenotype in metastatic disease.

Authors' Disclosures

C.A. Iacobuzio-Donahue reports research support from BMS. J. Xavier reports grants from NIH during the conduct of the study. No disclosures were reported by the other authors.

Authors' Contributions

D. Mathur: Conceptualization, data curation, software, formal analysis, funding acquisition, validation, investigation, visualization, writing–original draft, writing–review and editing. **C. Liao:** Software, visualization. **W. Lin:** Validation, investigation. **A. La Ferlita:** Software. **S. Alaimo:** Software, methodology. **S. Taylor:** Validation, investigation. **Y. Zhong:** Resources. **C. Iacobuzio-Donahue:** Resources. **A. Ferro:** Data curation, software, project administration. **J.B. Xavier:** Conceptualization, methodology, project administration, writing–review and editing.

Acknowledgments

This work was supported by NIH Research Program Grants under award numbers R01 CA266068, R01 CA229215, and U54 CA209975 to J.B. Xavier. D. Mathur was also supported by the Alan and Sandra Gerry Metastasis and Tumor Ecosystems Center (GMTEC) Gerry Fellowship and is currently supported by the NRSA fellowship. S. Aliaimo and A. La Ferlita are supported by MIUR PON research project BILIGeCT "Liquid Biopsies for Cancer Clinical Management" CUP B96G18000590005. The authors thank Joan Massague's lab for providing all the breast cancer cell lines used in this paper. They thank the Flow Cytometry core facility at MSKCC for sorting of our fluorescently-labeled cells. The authors also thank Justin Cross, Mirela Biresa, and Weige Qin from the Cell Metabolism core facility at MSKCC for help designing metabolic flux experiments, training on Seahorse equipment, and YSI analysis. The authors would like to acknowledge the American Association for Cancer Research and its financial and material support in the development of the AACR Project GENIE registry, as well as members of the consortium for their commitment to data sharing. Interpretations are the responsibility of study authors.

The Editor-in-Chief of *Cancer Research* is an author on this article. In keeping with AACR editorial policy, a senior member of the *Cancer Research* editorial team managed the consideration process for this submission and independently rendered the final decision concerning acceptability.

The publication costs of this article were defrayed in part by the payment of publication fees. Therefore, and solely to indicate this fact, this article is hereby marked "advertisement" in accordance with 18 USC section 1734.

Note

Supplementary data for this article are available at Cancer Research Online (http://cancerres.aacrjournals.org/).

Received January 16, 2023; revised June 12, 2023; accepted July 27, 2023; published first August 1, 2023.

References

1. Quail DF, Joyce JA. Microenvironmental regulation of tumor progression and metastasis. Nat Med 2013;19:1423–37.
2. Wu JM, Fackler MJ, Halushka MK, Molavi DW, Taylor ME, Teo WW, et al. Heterogeneity of breast cancer metastases: comparison of therapeutic target expression and promoter methylation between primary tumors and their multifocal metastases. Clin Cancer Res 2008;14:1938–46.
3. Solomayer EF, Diel IJ, Meyberg GC, Gollan C, Bastert G. Metastatic breast cancer: clinical course, prognosis and therapy related to the first site of metastasis. Breast Cancer Res Treat 2000;59:271–8.
4. Oliver AJ, Lau PKH, Unsworth AS, Loi S, Darcy PK, Kershaw MH, et al. Tissue-dependent tumor microenvironments and their impact on immunotherapy responses. Front Immunol 2018;9:70.
5. Deeb A, Haque S-U, Olowokure O. Pulmonary metastases in pancreatic cancer, is there a survival influence? J Gastrointest Oncol 2015;6:E48–51.
6. Minn AJ, Gupta GP, Siegel PM, Bos PD, Shu W, Giri DD, et al. Genes that mediate breast cancer metastasis to lung. Nature 2005;436:518–24.
7. Nguyen DX, Bos PD, Massagué J. Metastasis: from dissemination to organ-specific colonization. Nat Rev Cancer 2009;9:274–84.
8. Minn AJ, Kang Y, Serganova I, Gupta GP, Giri DD, Doubrovin M, et al. Distinct organ-specific metastatic potential of individual breast cancer cells and primary tumors. J Clin Invest 2005;115:44–55.
9. Paget S. The distribution of secondary growths in cancer of the breast. Lancet 1889;133:571–3.
10. Soni A, Ren Z, Hameed O, Chanda D, Morgan CJ, Siegal GP, et al. Breast cancer subtypes predispose the site of distant metastases. Am J Clin Pathol 2015;143:471–8.
11. Kennecke H, Yerushalmi R, Woods R, Cheang MCU, Voduc D, Speers CH, et al. Metastatic behavior of breast cancer subtypes. J Clin Oncol 2010;28:3271–7.
12. Smid M, Wang Y, Zhang Y, Sieuwerts AM, Yu J, Klijn JGM, et al. Subtypes of breast cancer show preferential site of relapse. Cancer Res 2008;68:3108–14.
13. Cummings MC, Simpson PT, Reid LE, Jayanthan J, Skerman J, Song S, et al. Metastatic progression of breast cancer: insights from 50 years of autopsies. J Pathol 2014;232:23–31.
14. Reiter JG, Makohon-Moore AP, Gerold JM, Heyde A, Attiyeh MA, Kohutek ZA, et al. Minimal functional driver gene heterogeneity among untreated metastases. Science 2018;361:1033–7.

15. Obenauf AC, Massagué J. Surviving at a distance: organ-specific metastasis. Trends Cancer 2015;1:76–91.
16. Dupuy F, Tabariès S, Andrzejewski S, Dong Z, Blagih J, Annis MG, et al. PDK1-dependent metabolic reprogramming dictates metastatic potential in breast cancer. Cell Metab 2015;22:577–89.
17. Warburg O, Wind F, Negelein E. The metabolism of tumors in the body. J Gen Physiol 1927;8:519–30.
18. Hanahan D. Hallmarks of cancer: new dimensions. Cancer Discov 2022;12:31–46.
19. Cailleau R, Young R, Olivé M, Reeves WJ. Breast tumor cell lines from pleural effusions 2. J Natl Cancer Inst 1974;53:661–74.
20. Puchalapalli M, Zeng X, Mu L, Anderson A, Hix Glickman L, Zhang M, et al. NSG mice provide a better spontaneous model of breast cancer metastasis than athymic (Nude) mice. PLoS One 2016;11:e0163521.
21. El-Mabhouh AA, Nation PN, Kaddoura A, Mercer JR. Unexpected preferential brain metastases with a human breast tumor cell line MDA-MB-231 in BALB/c nude mice. Vet Pathol 2008;45:941–4.
22. Bos PD, Zhang XH-F, Nadal C, Shu W, Gomis RR, Nguyen DX, et al. Genes that mediate breast cancer metastasis to the brain. Nature 2009;459:1005–9.
23. Kang Y, Siegel PM, Shu W, Drobnjak M, Kakonen SM, Cordón-Cardo C, et al. A multigenic program mediating breast cancer metastasis to bone. Cancer Cell 2003;3:537–49.
24. Basnet H, Tian L, Ganesh K, Huang Y-H, Macalinao DG, Brogi E, et al. Flura-seq identifies organ-specific metabolic adaptations during early metastatic colonization. eLife 2019;8:e43627.
25. Li AM, Ducker GS, Li Y, Seoane JA, Xiao Y, Melemenidis S, et al. Metabolic profiling reveals a dependency of human metastatic breast cancer on mitochondrial serine and one-carbon unit metabolism. Mol Cancer Res 2020;18:599–611.
26. Zhang J, Liu Q. Cholesterol metabolism and homeostasis in the brain. Protein Cell 2015;6:254–64.
27. Parpura V, Schousboe A, Verkhratsky A, editors. Glutamate and ATP at the interface of metabolism and signaling in the brain. Chambridge: Springer International Publishing; 2014.
28. McKeown SR. Defining normoxia, physoxia and hypoxia in tumours-implications for treatment response. Br J Radiol 2014;87:20130676.
29. Datta H, Stubbs WA, Alberti K. Substrate utilization by the lung. Metab Activ Lung 1980;85–104.
30. Lottes RG, Newton DA, Spyropoulos DD, Baatz JE. Lactate as substrate for mitochondrial respiration in alveolar epithelial type II cells. Am J Physiol Lung Cell Mol Physiol 2015;308:L953–61.
31. Zhong Y, Macgregor-Das A, Saunders T, Whittle MC, Makohon-Moore A, Kohutek ZA, et al. Mutant p53 together with TGFβ signaling influence organ-specific hematogenous colonization patterns of pancreatic cancer. Clin Cancer Res 2017;23:1607–20.
32. Alaimo S, Giugno R, Acunzo M, Veneziano D, Ferro A, Pulvirenti A. Post-transcriptional knowledge in pathway analysis increases the accuracy of phenotypes classification. Oncotarget 2016;7:54572–82.
33. Ritchie ME, Phipson B, Wu D, Hu Y, Law CW, Shi W, et al. limma powers differential expression analyses for RNA-sequencing and microarray studies. Nucleic Acids Res 2015;43:e47.
34. Mock A, Warta R, Dettling S, Brors B, Jäger D, Herold-Mende C. MetaboDiff: an R package for differential metabolomic analysis. Bioinformatics 2018;34:3417–8.
35. Balcarcel RR, Clark LM. Metabolic screening of mammalian cell cultures using well-plates. Biotechnol Prog 2003;19:98–108.
36. Ebrahim A, Lerman JA, Palsson BO, Hyduke DR. COBRApy: constraints-based reconstruction and analysis for python. BMC Syst Biol 2013;7:74.
37. Wagle N, Painter C, Krevalin M, Oh C, Anderka K, Larkin K, et al. The metastatic breast cancer project: a national direct-to-patient initiative to accelerate genomics research. JCO 2016;34:LBA1519.
38. Cerami E, Gao J, Dogrusoz U, Gross BE, Sumer SO, Aksoy BA, et al. The cBio cancer genomics portal: an open platform for exploring multidimensional cancer genomics data. Cancer Discov 2012;2:401–4.
39. Gao J, Aksoy BA, Dogrusoz U, Dresdner G, Gross B, Sumer SO, et al. Integrative analysis of complex cancer genomics and clinical profiles using the cBioPortal. Sci Signal 2013;6:pl1.
40. McInnes L, Healy J, Melville J. Umap: uniform manifold approximation and projection for dimension reduction. arXiv preprint arXiv:180203426. 2018.
41. AACR Project GENIE Consortium. AACR project GENIE: powering precision medicine through an international consortium. Cancer Discov 2017;7:818–31.
42. Chen M-T, Sun H-F, Zhao Y, Fu W-Y, Yang L-P, Gao S-P, et al. Comparison of patterns and prognosis among distant metastatic breast cancer patients by age groups: a SEER population-based analysis. Sci Rep 2017;7:9254.
43. Roshanzamir F, Robinson JL, Cook D, Karimi-Jafari MH, Nielsen J. Metastatic triple negative breast cancer adapts its metabolism to destination tissues while retaining key metabolic signatures. Proc Natl Acad Sci USA 2022;119:e2205456119.
44. Subramanian A, Tamayo P, Mootha VK, Mukherjee S, Ebert BL, Gillette MA, et al. Gene set enrichment analysis: a knowledge-based approach for interpreting genome-wide expression profiles. Proc Natl Acad Sci USA 2005;102:15545–50.
45. Mootha VK, Lindgren CM, Eriksson K-F, Subramanian A, Sihag S, Lehar J, et al. PGC-1alpha-responsive genes involved in oxidative phosphorylation are coordinately downregulated in human diabetes. Nat Genet 2003;34:267–73.
46. Alaimo S, Marceca GP, Ferro A, Pulvirenti A. Detecting disease specific pathway substructures through an integrated systems biology approach. Noncoding RNA 2017;3:20.
47. Chen J, Lee H-J, Wu X, Huo L, Kim S-J, Xu L, et al. Gain of glucose-independent growth upon metastasis of breast cancer cells to the brain. Cancer Res 2015;75:554–65.
48. Berg JM, Tymoczko JL, Stryer L. The glycolytic pathway is tightly controlled. Biochemistry 2002, 5th Edition. New York: W H Freeman.
49. DepMap Broad. [Internet]. This DepMap release contains data from CRISPR knockout screens from project Achilles, as well as genomic characterization data from the CCLE project. 2023 [cited 2023 May 25]. Available from: https://depmap.org/portal/.
50. Ghandi M, Huang FW, Jané-Valbuena J, Kryukov GV, Lo CC, McDonald ER, et al. Next-generation characterization of the Cancer Cell Line Encyclopedia. Nature 2019;569:503–8.
51. Jin X, Demere Z, Nair K, Ali A, Ferraro GB, Natoli T, et al. A metastasis map of human cancer cell lines. Nature 2020;588:331–6.
52. Hitosugi T, Chen J. Post-translational modifications and the Warburg effect. Oncogene 2014;33:4279–85.
53. Liberti MV, Locasale JW. The Warburg effect: how does it benefit cancer cells? Trends Biochem Sci 2016;41:211–8.
54. Carmona-Fontaine C, Bucci V, Akkari L, Deforet M, Joyce JA, Xavier JB. Emergence of spatial structure in the tumor microenvironment due to the Warburg effect. Proc Natl Acad Sci USA 2013;110:19402–7.
55. Itadani H, Mizuarai S, Kotani H. Can systems biology understand pathway activation? Gene expression signatures as surrogate markers for understanding the complexity of pathway activation. Curr Genomics 2008;9:349–60.
56. Mishra D, Banerjee D. Lactate dehydrogenases as metabolic links between tumor and stroma in the tumor microenvironment. Cancers (Basel) 2019;11:750.
57. Faubert B, Li KY, Cai L, Hensley CT, Kim J, Zacharias LG, et al. Lactate metabolism in human lung tumors. Cell 2017;171:358–71.
58. Carmona-Fontaine C, Deforet M, Akkari L, Thompson CB, Joyce JA, Xavier JB. Metabolic origins of spatial organization in the tumor microenvironment. Proc Natl Acad Sci USA 2017;114:2934–9.
59. Bonuccelli G, Tsirigos A, Whitaker-Menezes D, Pavlides S, Pestell RG, Chiavarina B, et al. Ketones and lactate "fuel" tumor growth and metastasis: Evidence that epithelial cancer cells use oxidative mitochondrial metabolism. Cell Cycle 2010;9:3506–14.
60. Fisher AB, Dodia C. Lactate and regulation of lung glycolytic rate. Am J Physiol 1984;246:E426–9.
61. Liu M, Quek L-E, Sultani G, Turner N. Epithelial-mesenchymal transition induction is associated with augmented glucose uptake and lactate production in pancreatic ductal adenocarcinoma. Cancer Metab 2016;4:19.
62. Magistretti PJ, Pellerin L, Martin JL. Brain energy metabolism: an integrated cellular perspective. New York: Raven Press; 1995.
63. Levine AJ, Puzio-Kuter AM. The control of the metabolic switch in cancers by oncogenes and tumor suppressor genes. Science 2010;330:1340–4.
64. McDonald OG, Li X, Saunders T, Tryggvadottir R, Mentch SJ, Warmoes MO, et al. Epigenomic reprogramming during pancreatic cancer progression links anabolic glucose metabolism to distant metastasis. Nat Genet 2017;49:367–76.
65. Davis RT, Blake K, Ma D, Gabra MBI, Hernandez GA, Phung AT, et al. Transcriptional diversity and bioenergetic shift in human breast cancer metastasis revealed by single-cell RNA sequencing. Nat Cell Biol 2020;22:310–20.
66. Lu X, Bennet B, Mu E, Rabinowitz J, Kang Y. Metabolomic changes accompanying transformation and acquisition of metastatic potential in a syngeneic mouse mammary tumor model. J Biol Chem. 2010;285:9317–21.